Supporting Information

Schreiber et al. 10.1073/pnas.1002538107

SI Text

Simulation Methods. ***Langevin equation.*** Writing the center of mass of dendral K as $\bar{\mathbf{R}}_K = \sum_{i\in K} l_i \mathbf{r}^i / \sum_{i\in K} l_i$ and defining its director $\bar{\mathbf{n}}_K$ as the director of the filament that forms its trunk, the dynamic evolution of the system may be described by one Langevin equation for all M dendrals,

$$\frac{\mathrm{D}}{\mathrm{D}t}\begin{pmatrix}\bar{\mathbf{R}}_1\\ \bar{\mathbf{n}}_1\\ \vdots\\ \bar{\mathbf{R}}_M\\ \bar{\mathbf{n}}_M\end{pmatrix} = \boldsymbol{\mu}\cdot\left[\begin{pmatrix}\mathbf{F}_1\\ \mathbf{T}_1\\ \vdots\\ \mathbf{F}_M\\ \mathbf{T}_M\end{pmatrix} + \begin{pmatrix}\mathbf{f}_1\\ \boldsymbol{\tau}_1\\ \vdots\\ \mathbf{f}_M\\ \boldsymbol{\tau}_M\end{pmatrix}\right]. \qquad [S1]$$

Here, $\mathbf{F}_K$ and $\mathbf{T}_K$ are the total deterministic forces and torques acting on dendral K, and $\mathbf{f}_K$ and $\boldsymbol{\tau}_K$ are the stochastic forces and torques that cause diffusion. The elements of the mobility matrix $\boldsymbol{\mu}$ are determined below, and the magnitudes of $\mathbf{f}_K$ and $\boldsymbol{\tau}_K$ are related to these values via the fluctuation-dissipation theorem. Denoting $\mathbf{V}_K = \mathrm{D}\bar{\mathbf{R}}_K/\mathrm{D}t$ and $\boldsymbol{\omega}_K = \mathrm{D}\bar{\mathbf{n}}_K/\mathrm{D}t$, we evolve the coordinates using Euler integration: $\bar{\mathbf{R}}_K(t+\mathrm{d}t) = \bar{\mathbf{R}}_K(t) + \mathbf{V}_K\mathrm{d}t$ and $\bar{\mathbf{n}}_K(t+\mathrm{d}t) = \boldsymbol{\omega}_K \times \bar{\mathbf{n}}_K(t)/|\boldsymbol{\omega}_K \times \bar{\mathbf{n}}_K(t)|$. Having determined the motion of the dendrals, we can compute the new positions and orientations of the individual filaments. For each filament $i \in K$ that constitutes dendral K, we update its director using $\mathbf{n}^i(t+\mathrm{d}t) = \boldsymbol{\omega}_K \times \mathbf{n}^i(t)/|\boldsymbol{\omega}_K \times \mathbf{n}^i(t)|$; to calculate its instantaneous center-of-mass velocity $\mathbf{v}^i$, we use $\mathbf{v}^i = \mathbf{V}_K + \boldsymbol{\omega}_K \times (\mathbf{r}^i - \bar{\mathbf{R}}_K)$, and thereby obtain $\mathbf{r}^i(t+\mathrm{d}t) = \mathbf{r}^i(t) + \mathbf{v}^i\mathrm{d}t$.

Mobility matrix of a dendral. The Langevin equation, Eq. **S1**, that describes the motion of the dendrals contains a block-diagonal mobility matrix $\boldsymbol{\mu}$ of the form

$$\boldsymbol{\mu} = \begin{pmatrix}\boldsymbol{\mu}_1 & 0 & \dots & 0\\ 0 & \boldsymbol{\mu}_2 & \dots & 0\\ \vdots & \vdots & \ddots & \vdots\\ 0 & 0 & \dots & \boldsymbol{\mu}_M\end{pmatrix}, \qquad [S2]$$

where the individual entries $\boldsymbol{\mu}_K$ are 6×6 matrices relating to individual dendrals. Here, we describe how to determine the elements of each matrix $\boldsymbol{\mu}_K$.

Consider a dendral K composed of unbranched filaments $i \in K$. Each of these filaments has a director $\mathbf{n}^i$, a length l_i, and a diameter b. When moving at a velocity $\mathbf{v}^i$, filament i experiences a drag force

$$\mathbf{F}^i_{\mathrm{drag}} = (\zeta^i_{\parallel}\mathbf{n}^i \otimes \mathbf{n}^i + \zeta^i_{\perp}(\mathsf{I} - \mathbf{n}^i \otimes \mathbf{n}^i))\cdot \mathbf{v}^i, \qquad [S3]$$

where I is the identity matrix and $\mathbf{a}\otimes\mathbf{b}$ denotes the matrix with elements $a_i b_j$, i.e., the outer vector product. The product $\mathbf{n}^i \otimes \mathbf{n}^i$ acts as a projection operator onto the direction of the rod, and $\zeta^i_{\parallel}$ and $\zeta^i_{\perp}$ are, respectively, the viscous drag coefficients for motion parallel and perpendicular to the rod's axis, given by the expressions (S1)

$$\zeta^i_{\parallel} = \frac{2\pi\eta_s l_i}{\ln(l_i/b)}, \qquad [S4]$$

and

$$\zeta^i_{\perp} = \frac{4\pi\eta_s l_i}{\ln(l_i/b)}, \qquad [S5]$$

where η_s is the viscosity of the cytosol. Similarly, filament i experiences a drag torque

$$\mathbf{T}^i_{\mathrm{drag}} = (\zeta^i_{r,\perp}(\mathsf{I} - \mathbf{n}^i \otimes \mathbf{n}^i) + \zeta^i_{r,\parallel}\mathbf{n}^i \otimes \mathbf{n}^i)\cdot\boldsymbol{\omega}_K, \qquad [S6]$$

due to the rotation of the dendral at angular velocity $\boldsymbol{\omega}_K$, where $\zeta^i_{r,\parallel}$ and $\zeta^i_{r,\perp}$ are, respectively, the drag coefficients for rotation of a rod about its axis and perpendicular to its axis, given by the expressions (S1)

$$\zeta^i_{r,\parallel} = 4\pi\eta_s R^2 l_i, \qquad [S7]$$

and

$$\zeta^i_{r,\perp} = \frac{\pi\eta_s l_i^3}{3(\ln(l_i/b) - \gamma)}, \qquad [S8]$$

with $\gamma \approx 0.8$.

The total drag force $\mathbf{F}_{\mathrm{drag},K}$ and the total drag torque $\mathbf{T}_{\mathrm{drag},K}$ acting on dendral K are then

$$\mathbf{F}_{\mathrm{drag},K} = \sum_{i\in K}\mathbf{F}^i_{\mathrm{drag}}, \qquad [S9]$$

and

$$\mathbf{T}_{\mathrm{drag},K} = \sum_{i\in K}\mathbf{T}^i_{\mathrm{drag}} + (\mathbf{r}^i - \bar{\mathbf{R}}_K)\times\mathbf{F}^i_{\mathrm{drag}}, \qquad [S10]$$

and, by writing the velocities $\mathbf{v}^i$ of the individual filaments in terms of the velocity $\mathbf{V}_K$ and angular velocity $\boldsymbol{\omega}_K$ of the dendral using

$$\mathbf{v}^i = \mathbf{V}_K + \boldsymbol{\omega}_K \times (\mathbf{r}^i - \bar{\mathbf{R}}_K), \qquad [S11]$$

we obtain both the drag force and the drag torque acting on the dendral as linear functions of $\mathbf{V}_K$ and $\boldsymbol{\omega}_K$, i.e.,

$$\begin{pmatrix}\mathbf{F}_{\mathrm{drag},K}\\ \mathbf{T}_{\mathrm{drag},K}\end{pmatrix} = \boldsymbol{\Gamma}_K\begin{pmatrix}\mathbf{V}_K\\ \boldsymbol{\omega}_K\end{pmatrix}, \qquad [S12]$$

with a 6×6 drag matrix $\boldsymbol{\Gamma}_K$. Aside from Brownian fluctuations, the drag force and drag torque must balance the total contact force $\mathbf{F}_K$ and contact torque $\mathbf{T}_K$ acting on the dendral. Thus referring to Eq. **1**, the mobility matrix in Eq. **2** is simply the inverse of the drag matrix,

$$\boldsymbol{\mu}_K = \boldsymbol{\Gamma}_K^{-1}. \qquad [S13]$$

Stochastic forces and torques. The stochastic Brownian force $\mathbf{f}_K$ and torque $\boldsymbol{\tau}_K$ acting on dendral K may be obtained from the drag matrix $\boldsymbol{\Gamma}_K$ by using the fluctuation–dissipation relations

$$\langle f_{K,\alpha} f_{K',\beta}\rangle = 2k_{\mathrm{B}}T\Gamma_{K,\alpha\beta}\delta_{KK'}, \qquad [S14]$$

$$\langle \tau_{K,\alpha} f_{K',\beta}\rangle = 2k_{\mathrm{B}}T\Gamma_{K,\alpha+3\,\beta}\delta_{KK'}, \qquad [S15]$$

and

$$\langle \tau_{K,\alpha} \tau_{K',\beta} \rangle = 2k_B T \Gamma_{K,\alpha+3\,\beta+3} \delta_{KK'}. \quad \textbf{[S16]}$$

Here, the Greek subscripts label the element of the vector, i.e., the x, y, or z coordinate, and the adjustment "+3" ensures that the component of the matrix corresponds to the torque, rather than the force.

Simulation Results. ***Lamellipod height.*** We found that the lamellipod height was almost independent of the force F_T applied to the top wall of the box representing the lamellipod, provided that $F_T > 10$ pN. Fig. S2 shows how the height of the lamellipod varies as a function of the external retarding force.

Retrograde flow. In Fig. S1, we plot the protrusion speed v_F vs. the retrograde flow speed v_R. Note that v_F decreases as v_R increases, as expected if expansion of the actin gel drives both the retrograde flow and the protrusion. In Fig. S7, we plot the retrograde flow speed v_R of the center of mass of F-actin within discrete volume elements, as a function of distance from the leading edge. When filament–filament interactions are turned off, the retrograde flow differs only marginally from zero and the spatial extent of the filament network is significantly reduced compared to our normal case where excluded volume effects are taken into account.

Filament orientation. At the leading edge of the lamellipod, the rate of nucleation of new branches on an existing filament is dependent on the filament orientation. As a consequence, there is a preferential orientation of filaments within a branched network. We found that the most likely orientation of filaments was at $\pm$(35–40)° to the z direction; the probability density at these angles was approximately twice what would be expected were filaments randomly oriented. This self-organized structure of the branched network is consistent with microscopic studies that have revealed an apparent long-range diagonal actin meshwork (S3). We found, however, that the global order of branched networks, as measured by the nematic order parameter S of the filaments, was slight: $S \approx 0.06$ at low load and $S \approx 0.10$ at the stall force. By contrast, for unbranched networks, we found $S \approx 0.13$ at low loads and $S \approx 0.17$ at the stall force, with a tendency for filaments to align parallel to the leading edge; such nematic ordering clearly compromises the ability of actin polymerization to generate motility, either by a Brownian ratchet mechanism, or by gel expansion.

Robustness to choice of Arp2/3 activation model. In Fig. S3, we show how the force–velocity curve depends on the precise model of Arp2/3 activation chosen. The box model is the default model used in our simulation, with branching occurring at rate $k_{br} = 1.4 \cdot 10^{-5}/(\text{s.u. s})$ in a box of height $\Delta_y = 50$ nm and width $\Delta_z = 10$ nm at the base of the leading edge. The stepwise model uses three adjacent boxes of height $\Delta_y = 50$ nm and width $\Delta_z = 5$ nm, with the branching rate declining successively from $k_{br} = 1.5 \cdot 10^{-5}/(\text{s.u. s})$ to $k_{br} = 1.0 \cdot 10^{-5}/(\text{s.u. s})$ to $k_{br} = 0.5 \cdot 10^{-5}/(\text{s.u. s})$, and with filament nucleation occurring only in the box closest to the front. In the exponential model, the branching rate is described by $k_{br} = k_{br}^0 \exp(-d/\lambda)$, where d is the distance of the actin subunit (s.u.) under consideration from the base of the leading edge, $\lambda = 12$ nm and $k_{br}^0 = 1.4 \cdot 10^{-5}/(\text{s.u. s})$. The form of the force–velocity curve is the same for these different activation models. This robustness to model detail is important as the precise mode of Arp2/3 activation is still a matter of some debate.

Robustness to variation of parameters. In our standard simulation, there was no filament severing ($k_{sever} = 0$). We investigated whether finite values of k_{sever} modified the force–velocity relation. As shown in Fig. S4, it is reassuring that for plausible values of the severing rate, $k_{sever} \leq 10^{-3}/(\text{s.u.s})$, the force–velocity relation is unchanged. Remarkably, even at an unrealistically high value $k_{sever} = 10^{-4}/(\text{s.u.s})$, for which the rapid dismantling of dendrals causes the spatial extent of the lamellipod to be severely diminished, the qualitative form of the force–velocity relation is maintained.

We conducted extensive simulations to examine how variation of the parameters governing actin kinetics affect the force–velocity relation. As shown in Fig. S5, the qualitative form of the force–velocity relation remained the same as individual parameters were varied from about a quarter to four times their default value.

Although the general characteristics of the motile behavior were insensitive to parameter variation, the choice of kinetic parameters did have an effect on individual quantities, such as the protrusion speed, stall force, and lamellipod height. In Fig. S6, we show the influence of varying the parameters on the protrusion speed v_F of the leading edge.

Simplified Model of Motility Generated by a Swelling Actin Gel. ***Expansion speed of a gel of growing dendrals.*** Within our model lamellipod, actin filaments grow at rate k_+^0 and are capped at rate k_{cap}, so their typical length is

$$\langle l \rangle = k_+^0 l_{mon}/k_{cap}. \quad \textbf{[S17]}$$

We suppose that the filaments are randomly packed as tightly as possible. Then the typical F-actin concentration $[F]$ may be estimated from the theoretical expression for the packing efficiency ϕ of randomly aligned rods, given by (S2)

$$\phi = \langle c \rangle / \alpha, \quad \textbf{[S18]}$$

where α is the aspect ratio of the rods and $\langle c \rangle$ is the mean number of contacts that each rod makes with others, which has been found to have the value $\langle c \rangle \approx 5.4$ (S2). Taking the F-actin monomer volume to be $V_{mon} = \pi l_{mon} (b/2)^2$, this gives

$$[F] = \frac{4 \langle c \rangle k_{cap}}{\pi k_+^0 l_{mon}^2 b}. \quad \textbf{[S19]}$$

For the default parameter values used in the simulation, Eq. **S19** yields $[F] = 0.39$ mM, in good agreement with the maximal filament density in Fig. 3.

Consider now the number of growing filaments, N_+, in a small volume V adjacent to the leading edge. More such filaments are created by branching and by nucleation, but filaments also stop growing as a consequence of capping. Thus

$$\frac{dN_+}{dt} = k_{br} N_b + k_N - k_{cap} N_+, \quad \textbf{[S20]}$$

where N_b is the total number of F-actin monomers to which Arp2/3 can bind and k_N is the nucleation rate at the leading edge. We estimate $N_b = [F] L_x \Delta_y \Delta_z$, where L_x is the breadth of the box representing the lamellipod. Supposing we have a quasi-steady state so that the number of growing filaments within the volume V is constant, i.e., $dN_+/dt = 0$, we have

$$N_+ = (k_{br} N_b + k_N)/k_{cap}, \quad \textbf{[S21]}$$

and the rate at which F-actin monomers are added to the gel as a result of both growth and nucleation is then

$$\frac{dN}{dt} = k_+^0 N_+ + k_N = \frac{k_0^+ (k_{br} N_b + k_N)}{k_{cap}} + k_N. \quad \textbf{[S22]}$$

This additional material will, through excluded volume interactions, cause the gel to expand in the z direction at speed

$$v_{\text{exp}} = \frac{1}{[F]L_x\Delta_y}\frac{\mathrm{d}N}{\mathrm{d}t}, \qquad \textbf{[S23]}$$

which, together with Eq. **19** gives

$$v_{\text{exp}} = \frac{k_{\text{br}}k_+^0\Delta_z}{k_{\text{cap}}} + \frac{(k_+^0 + k_{\text{cap}})\rho_{\text{nuc}}\pi l_{\text{mon}}^2 b k_+^0}{4\langle c\rangle k_{\text{cap}}^2}, \qquad \textbf{[S24]}$$

where $\rho_{\text{nuc}} = k_N/L_x\Delta_y$ is the nucleation density at the leading edge.

Note that the validity of the simplifications made above breaks down when $k_+^0 \to 0$, because then the filaments are too short to pack closely. Also, the assumption of approximately constant F-actin concentration $[F]$ within the volume V is invalid when $k_{\text{cap}} \to 0$, because then the filaments grow for a long duration, leading to a strong spatial variation of filament length and, consequently, packing density.

Reaction force of adhesions due to retrograde flow. The expansion of the portion of the network adjacent to the leading edge at speed v_{exp} causes forward motion of the leading edge at speed v_F and retrograde flow of the dendrals in the anterior portion of the lamellipod at speed v_R. Some of the dendrals in this rear section are adhered to the substrate and the elastic adhesions become increasingly strained as the network is propelled backward, until eventually they detach. As a result, the substrate exerts an adhesive stress on the network, which balances any external load F_{ext} that might oppose the motion of the leading edge.

To determine the adhesive stress, we first calculate the probability $p(t)$ that an adhesion which was formed at time t_0 is still attached at time $t_0 + t$. We have

$$\frac{\mathrm{d}p}{\mathrm{d}t} = -k_{\text{off}}p. \qquad \textbf{[S25]}$$

where the strain-dependent detachment rate k_{off} is given by Eq. **S2**, reproduced here as follows:

$$k_{\text{off}} = k_{\text{off}}^0 \exp\left(\frac{\kappa a|\mathbf{x}|}{k_BT}\right), \qquad \textbf{[S26]}$$

where $\mathbf{x}$ is the vector linking the two ends of the spring describing the adhesion. Owing to the retrograde flow, $|\mathbf{x}| = \sqrt{v_R^2t^2 + y_0^2}$, where y_0 is some average initial strain. Thus

$$p(t) = \exp\left[-\int_0^t k_{\text{off}}^0 \exp\left(\frac{\kappa a\sqrt{v_R^2\xi^2 + y_0^2}}{k_{\text{B}}T}\right)\mathrm{d}\xi\right]. \qquad \textbf{[S27]}$$

The mean lifetime $\bar{t}$ of an adhesion is then

$$\bar{t} = \int t\mathrm{d}p, \qquad \textbf{[S28]}$$

and the mean reactive force exerted by a single adhesion is

$$\bar{F}_{\text{adh}} = \frac{1}{2}\kappa v_R\bar{t}. \qquad \textbf{[S29]}$$

For the case $y_0 = 0$, this expression may be calculated analytically, giving

$$\bar{F}_{\text{adh}} = \frac{k_{\text{B}}T}{a}e^{\gamma}\Gamma(0,\gamma), \qquad \textbf{[S30]}$$

with

$$\gamma = \frac{k_{\text{B}}Tk_{\text{off}}^0}{\kappa a v_R} \qquad \textbf{[S31]}$$

and

$$\Gamma(\alpha,\beta) = \int_\beta^\infty t^{\alpha-1}e^{-t}\mathrm{d}t \qquad \textbf{[S32]}$$

being the upper incomplete gamma function; but to provide a better match to our simulation we evaluate the expression numerically for the case $y_0 = \Delta_{\text{adh}}/2$.

The above analysis indicates that at low retrograde flow speeds, each adhesion generates an effective drag of constant, high value—the so-called "protein friction" (S4). Consequently, the average reactive force due to an adhesion increases steeply and linearly as the flow speed increases. At high retrograde flow speeds, on the other hand, each adhesion typically gets forcibly detached once it has been stretched through a characteristic distance. Consequently, the average reactive force that it generates tends toward a constant value, independent of the retrograde flow speed.

In the simulation, we observed that the total number of adhesions, N_{adh}, remained approximately constant, independent of the load F_{ext} applied to the leading edge. With this assumption, we have for the balance of forces

$$F_{\text{ext}} = N_{\text{adh}}\bar{F}_{\text{adh}}. \qquad \textbf{[S33]}$$

Eqs. **29** and **33** together give F_{ext} as a function of v_R. A knowledge of the relation between the protrusion speed v_F and the speed of retrograde flow v_R then gives v_F as a function of F_{ext}, i.e., the force–velocity relation. In Fig. S8, we plot the force–velocity relation using the dependence of v_F on v_R observed in Fig. S1. For comparison, we also show the case $v_{\text{exp}} = v_F + v_R$ (which holds at low forces), with v_{exp} extrapolated from Fig. S1 for $v_R = 0$.

Values of parameters describing adhesions The values of the parameters characterizing the adhesions were chosen to match experimental observations, where possible. Thus the value for k_{off}^0 was chosen so that the typical lifetime of an adhesion, from Eq. **28**, is 0.5 s (S5) when the retrograde flow speed is $v_R = 1$ μm/min. The value for k_{on} was determined by adjusting its value so that the stress profiles obtained in the simulation match those measured experimentally (S6). The length scale a was chosen to be the size of a typical protein domain and we checked that the results did not depend critically on the precise value.

1. Doi M, Edwards SF (1986) *The Theory of Polymer Dynamics*. Clarendon Press, Oxford, pp 324–380.
2. Williams SR, Philipse AP (2003) Random packings of spheres and spherocylinders simulated by mechanical contraction. *Phys Rev E* 67:051301.
3. Verkhovsky AB, et al. (2003) Orientation order of the lamellipodial actin network as demonstrated in living motile cells. *Mol Biol Cell* 14:4667–4675.
4. Tawada K, Sekimoto K (1991) Protein friction exerted by motor enzymes through a weak-binding interaction. *J Theor Biol* 159:193–200.
5. Matthews BD, et al. (2004) Mechanical properties of individual focal adhesions probed with a magnetic microneedle. *Biochem Biophys Res Commun* 313:758–764.
6. Oliver T, Dembo M, Jacobson K (1999) Separation of propulsive and adhesive traction stresses in locomoting keratocytes. *J Cell Biol* 145:589–604.

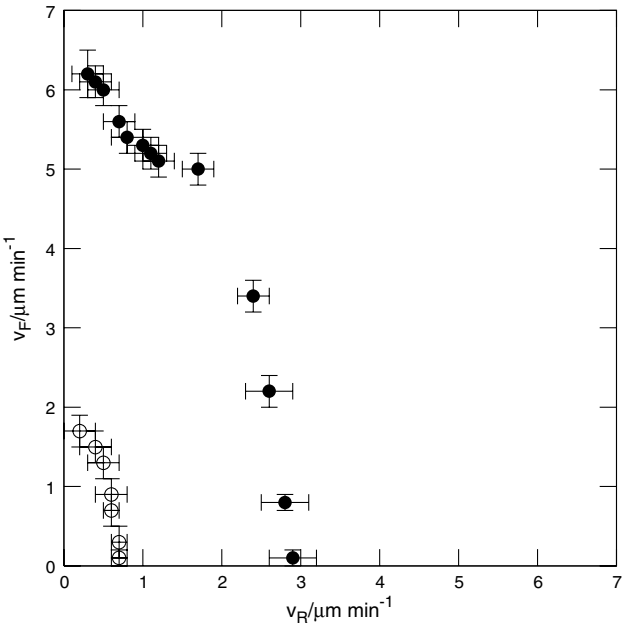

Fig. S1. Protrusion speed v_F as a function of the retrograde flow speed v_R for both branched (○) and unbranched rods (●).

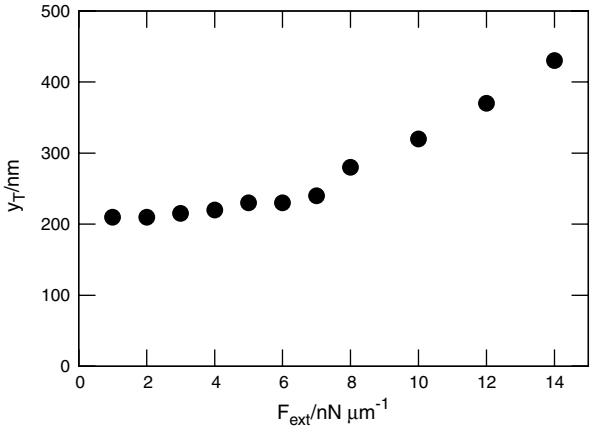

Fig. S2. Height y_T of the lamellipod as a function of the external retarding force, for branched rods.

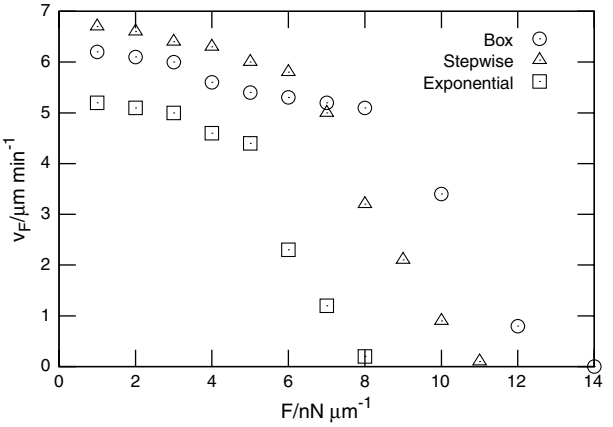

Fig. S3. Force–velocity relation for different Arp2/3 activation models.

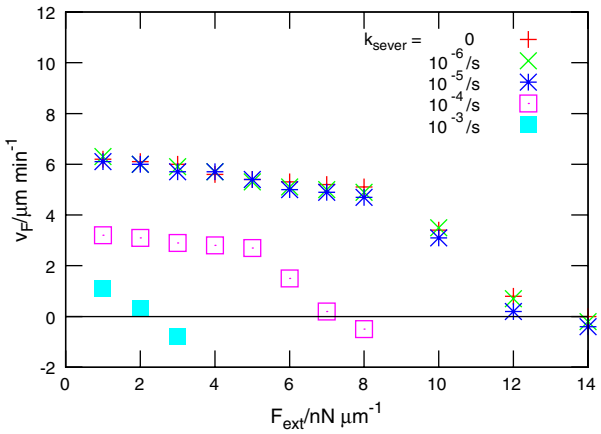

Fig. S4. Force–velocity relation for different severing rates k_{sever}.

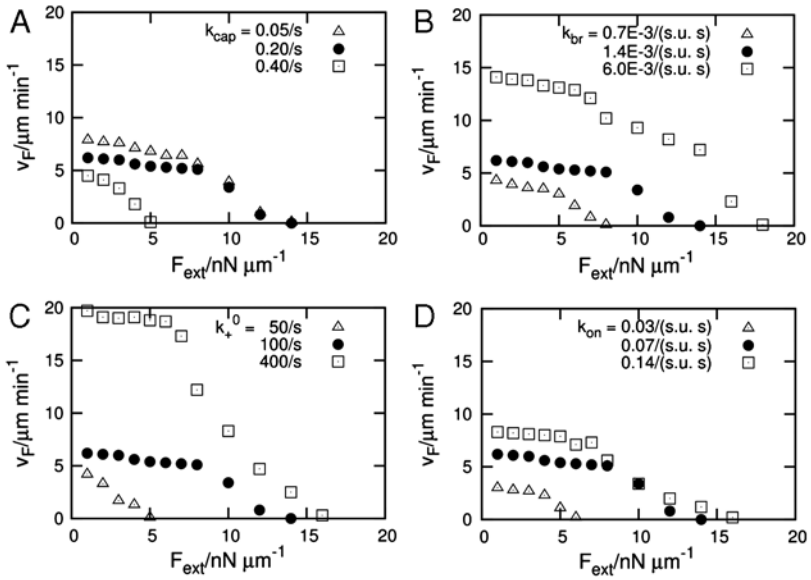

Fig. S5. Force–velocity relation for different values of the simulation parameters: variation of (*A*) capping rate k_{cap}, (*B*) branching rate k_{br}, (*C*) growth rate k_{+}^{0}, and (*D*) attachment formation rate k_{on}.

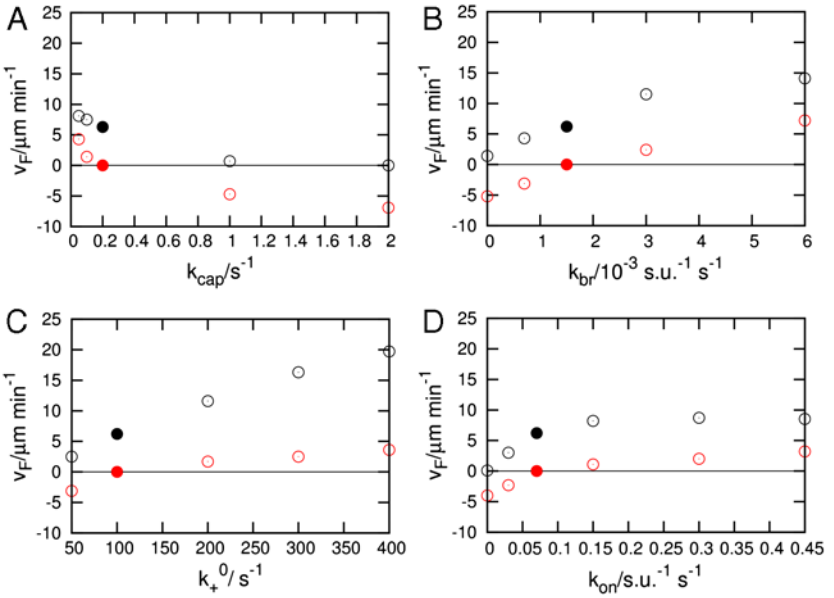

Fig. S6. Parameter dependence of the protrusion speed v_F for two different retarding forces F_{ext} per unit lamellipodial width (black open data, $F_{ext} = 1$ nN/µm; red open data, $F_{ext} = 14$ nN/µm, which corresponds to the stall force for the default set of parameter values). Filled circles correspond to the default value of the varied parameter. Variation of (*A*) capping rate, (*B*) branching rate, (*C*) polymerization rate, and (*D*) rate of forming adhesions.

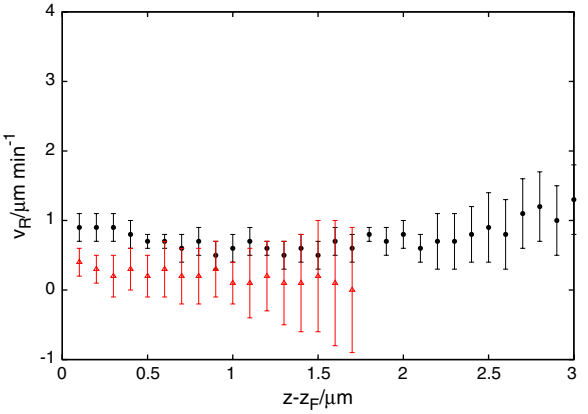

Fig. S7. Retrograde flow profiles for both interacting (black data) and noninteracting dendrals (red data).

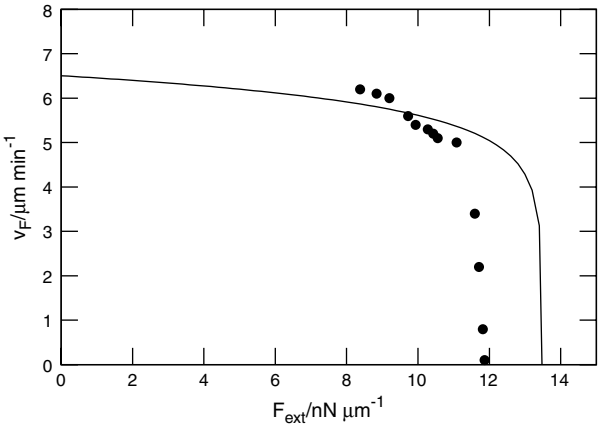

Fig. S8. Force–velocity relation according to the simplified analytical model. Data points (•) correspond to the relation between v_F and v_R shown in Fig. S1, whereas the line corresponds to $v_F + v_R = v_{exp} = 6.5$ µm min^{-1}, which is a good approximation to the data in Fig. S1 for $v_F > 5$ µm min^{-1}.

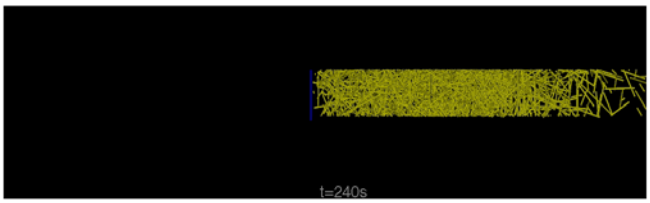

Movie S1. Dynamics of a model lamellipod powered by the polymerization of dendrals. The simulation box is viewed from above the substrate and the blue plane indicates the position of the movable front wall that represents the leading edge.

Movie S1 (MPG)